



## Statistical analogies between earthquakes, micro-quakes in metals and avalanches in the 1D Burridge-Knopoff model

András Kuki<sup>1</sup> , Sándor Lipcsei<sup>2</sup> , István Gere<sup>1</sup> , Ferenc Járari-Szabó<sup>1</sup> ,  
Attila Gergely<sup>1</sup> , Dávid Ugi<sup>2</sup> , Péter Dusán Ispánovity<sup>2</sup> , Zoltán Dankházi<sup>2</sup> ,  
István Groma<sup>2</sup>  and Zoltán Néda<sup>1</sup> 

<sup>1</sup> Physics Department, Babeş-Bolyai University, Cluj-Napoca, Romania

<sup>2</sup> Department of Materials Physics, Eötvös Loránd University, Budapest, Hungary

*Received 24 March 2022, in final form 27 March 2023*

Universalities and intriguing analogies in the statistics of avalanches are revealed for three physical systems defined on largely different length and energy scales. Earthquakes induced by tectonic scale dynamics, micro-scale level quakes observed from slipping crystallographic planes in metals and a one-dimensional, room-scale spring-block type Burridge-Knopoff model is studied from similar statistical viewpoints. The validity of the Gutenberg-Richter law for the probability density of the energies dissipated in the avalanches is proven for all three systems. By analysing data for three different seismic zones and performing acoustic detection for different Zn samples under deformation, universality for the involved scaling exponent is revealed. With proper parameter choices the 1D Burridge-Knopoff model is able to reproduce the same scaling law. The recurrence times of earthquakes and micro-quakes with magnitudes above a given threshold present again similar distributions and striking quantitative similarities. However, the 1D Burridge-Knopoff model cannot account for the correlations observed in such statistics.

*Keywords:* earthquakes, micro-plasticity, avalanches, universalities, scaling, correlations, Burridge-Knopoff model

### 1. Introduction

Earthquakes are serious threats to humanity (Lewis, 2005), large earthquakes can easily destroy cities, killing thousands of people and causing inestimable social and economic damage. Nowadays there are two main directions for minimizing the destructive power of earthquakes by attempting predictions for their appearance: (1) searching for precursors of large earthquakes or (2) achieving a better statistical understanding that would allow a useful probabilistic risk

evaluation. While the first direction is largely debated in the scientific community (Conti et al., 2022; Picozza et al., 2021), everybody agrees on the usefulness of a statistical understanding of the observed events. Interesting statistical laws have been revealed during the past century. The famous Gutenberg-Richter law (Gutenberg and Richter, 1944; Gutenberg and Richter, 1956) and Omori law (Utsu, 1961; Utsu et al., 1961) are well-known examples in such a sense. Although, these laws have been confirmed in many seismologically active zones and geographical regions of different sizes, the use of different scales on which the strength of the earthquakes were measured and the incompleteness of the data were serious impediment to directly compare scaling exponents. Universalities in the relevant scaling exponents could offer however additional clues toward a more complete statistical description.

Striking analogies of the Gutenberg-Richter and Omori laws for earthquakes with the statistics observed in other avalanche-like phenomena catalyzed the development of the field of Self-Organized Criticality (SOC). For the dynamics of an ensemble of particles avalanches are defined, as a sudden increase in their flow or collective displacement. Avalanche-like phenomena are considered those processes where the dynamics of the system is dominated by such events. In SOC the physical system converges to a dynamically steady-state, characterized with energy dissipation events (in form of avalanches) having a power-law like distribution in their sizes (Bak et al., 1988; Bak and Chen, 1991). Some basic models of modern physics have been developed for exemplifying SOC. One could mention in this sense the famous sand-pile model (Bak et al., 1987) or the spring-block model of Burridge and Knopoff (Burridge and Knopoff, 1967). The Burridge-Knopoff model was the first one to incorporate realistic elements for the frictional movement of the tectonic plates that successfully reproduced the Gutenberg-Richter law for the earthquake magnitude distribution. Aided by the spectacular development in our computational resources, this model is still under investigation in computational physics studies (Mori and Kawamura, 2006; Mori and Kawamura, 2008).

Lately, an interesting similarity was reported with mechanically analog micro-scale quakes, where one can observe and measure energy dissipations in sliding crystallographic planes (Ispánovity et al., 2022). In the first half of the 20<sup>th</sup> century Orován, Taylor and Polányi were the first to understand the basic mechanism of plastic deformation of metals (Orowan, 1934; Polanyi, 1934; Taylor, 1934), namely, the concept of dislocation movement during shear deformation of crystals. However, in a direct manner, dislocation dynamics was not studied thoroughly until the discovery of electron microscopy. Since then, many interesting phenomena were observed related to the collective behavior of dislocations, such as the dislocation pattern formation (Groma, 2000), Portevin-Le Chatelier (PLC) effect (Dierke et al., 2007), effect of dislocations on semiconductor properties (Hirsch, 1985), etc. The complementary acoustic emission study of dislocation movement started two decades ago with the compressions of ice crystals by

Miguel et al. (Miguel, 2006). Nevertheless, in the following years the extensive improvement of the field resulted in the development of fabrication of micropillars in metals via focused ion beam technology (Dimiduk et al., 2005; Dimiduk et al., 2006), in-situ compressions (Kalácska et al., 2020; Zoller et al., 2020) and concurrent acoustic emission measurements (Hegyí et al., 2017; Ispánovity et al., 2022).

The present work offers a unified, pedagogical discussion on the avalanche-like statistics in three different processes: earthquakes at tectonic and micro-scale level and the dynamics of a simple Burridge-Knopoff-type model. We attempt to show quantitative analogies between the related phenomena and discuss some aspects for probabilistic predictions. By reprocessing the available earthquake catalogs, three different tectonic zones (Romania, Southern-California and Japan) are studied statistically. The data is unified by transforming all magnitudes to energy scale, allowing to reveal further universalities in the statistics. This methodology offers a novel perspective to some already known empirical laws. For the micro-scale level quakes observed in compressed micropillars the same statistical analyses are performed and interesting analogies with earthquakes are discussed. For a unified modelling of the statistics observed in both the macro and micro-level quakes we use the simple one-dimensional Burridge-Knopoff model. During this computational exercise we successfully reproduce some previously known results, and study the model critically from novel perspectives. We conclude on the applicability of this simple modeling paradigm and discuss on possibilities for improving it.

## 2. Earthquakes and their statistics

### 2.1. Magnitude scales

The magnitude of an earthquake (Ohnaka, 2013; Bornmann and Saul, 2011) is meant to represent the cumulative strength of it. The usual definition is that “it is a number that characterizes the relative earthquake size” (Bornmann and Saul, 2009) or “a number that characterizes the relative size or amount of elastic energy released by such an event” (Bornmann and Saul, 2011). It should not be confused with the intensity, which is the severity/degree of ground shaking and its impact on people, buildings and surroundings. During the past many different magnitude scales have been elaborated. Most of the magnitude scales are based on the measurement of a particular property of the seismic wave. This property can be the maximal amplitude, the length of the signal, frequency etc. One of the earliest magnitude scales was the Richter-scale, and even nowadays this is among the most popular (Richter, 1935). The moment magnitude scale ( $M_w$ ) is however the one that characterizes in the best manner the total emitted energy during an earthquake (Hanks and Kanamori, 1979). We will use this magnitude in our statistics. It can be defined as

$$M_w = \frac{2}{3} [\log_{10}(M_0) - 9.1], \quad (1)$$

where  $M_0$  (in units of N.m) represents the required mechanical work to generate the slipping of the respective rupture (Bormann and Dewey, 2014). More precisely  $M_0 = \mu AD$ , where  $\mu$  is the shear modulus of the respective rock,  $D$  is the measure of the slip of the two sides of the rupture (average slip) and  $A$  is the surface area of the fissure.  $M_0$  represents the radiated seismic energy of the earthquake and from here on it will be denoted with  $E$ , because we are focusing only on scaling properties. From Eq. (1) the empiric relation between the moment magnitude ( $M_w$ ) and the total energy ( $E$ ) follows as:

$$E \sim 10^{1.5M_w} \quad (2)$$

## 2.2. Statistical laws

We shortly review here some well-known statistical laws for earthquakes.

The **Gutenberg-Richter law** quantifies an empiric finding concerning the magnitude distribution of earthquakes: for a given seismic region and time interval (Gutenberg and Richter, 1956a,b) the number of earthquakes ( $N$ ) with magnitude above a level  $M$  can be given as:

$$N = N_{tot} \cdot 10^{-bM}, \quad (3)$$

with the value of  $b$  around 1 (El-Isa, 2018). Here  $N_{tot}$  stands for the total number of earthquakes within the statistics.

The **Omori law** gives a relation between the rate of aftershocks produced after a main shock, and the  $t$  time elapsed from the main shock (Utsu, 1961; Utsu et al., 1961):

$$n(t) = \frac{k}{(c+t)^p}, \quad (4)$$

Here  $n(t)$  is the rate of the aftershock occurrence,  $k$  and  $c$  are characteristic parameters of the given aftershock sequence and  $p$  is an exponent, governing the rate of decrease. Usually the value of  $p$  is in the interval 0.7–1.5. This law suggests the temporal clustering for the aftershocks of an earthquake. The fact that the rate of the aftershock occurrence follows a power law, implies that the relaxation process does not have a characteristic time-scale. Furthermore, the presence of the power law implies also the presence of temporal correlations in the statistics.

Following on the time-like distribution of earthquakes, recently an interesting statistical law was revealed for **the recurrence time distribution** (Corral, 2006). Assuming a fixed magnitude threshold  $M_c$ , one can look for the time-interval distribution between events with magnitude greater than  $M_c$ . It was found that the time intervals  $t$  between such events are well approximated with a Gamma distribution:

$$\rho(t) = \frac{\beta^\alpha}{\Gamma(\alpha)} t^{\alpha-1} e^{-\beta t}. \quad (5)$$

The  $\alpha$  and  $\beta$  parameters of the distribution depend on the chosen  $M_c$  threshold and investigated seismic region.

### 2.3. Earthquake data mining and processing

In the present work we first reconsidered the above discussed statistical laws, searching for further universalities. For our statistical studies on earthquakes three seismic regions were considered: the Vrancea tectonic zone (Romania), Southern-California and Japan. The primary reason for selecting these seismic zones were our access to their long-term, good resolution and documented earthquake data.

The Vrancea seismic zone generates crustal and intermediate-depth earthquakes (Tugui et al., 2009), and the nature of the seismogeneity is still debated (Radulian, 2015; Bokelmann and Rodler, 2014). The seismic activity in Southern California are caused by the relative (lateral) movement of the Pacific and North American plates. The largest part of the displacement is in the San Andreas fault and other faults parallel with this: the San Jacinto, Elsinore, and Imperial faults. The majority of earthquakes occur at depths from 1 to 30 km (Topozada, 2004). Japan is probably the most known seismic hotspot, where many historical seismicity data is well documented and modern time data are recorded with great accuracy (Matsu'ura, 2017). The Japanese archipelago is located in an active zone where four lithospheric plates are in interaction, and as a result of this various types of earthquakes with different depths are generated.

In order to assure the completeness of the data and statistical consistency, only earthquakes with magnitudes ( $M_w$ ) of at least 2.5 were considered, a limit for which the catalogues are believed to be accurate. (Wiemer and Wyss, 2000; Moldovan et al., 2005; Hutton et al., 2010). This also eliminates many magnitude measurement errors that affects mainly the smaller and abundant earthquakes. No spatial filters were considered; therefore all earthquakes present in the database were used in the statistics. However, in order to have a clear separation of the different events, we also introduced a time-like cutoff in the data. If the elapsed time between two consecutive earthquakes did not exceed 10 seconds, only the one with the greater magnitude was kept. In such manner we intended to assure that our data surely indicate clearly separable earthquakes, although some earthquakes that have very different epicenter but are simultaneous with the selected one, are lost. This simplification could affect therefore in a tiny manner the magnitude statistics for Japan. It is important to emphasize also the fact that we did not consider any differentiation between fore-, after- and main shocks. Instead of the individual events, we focus therefore rather on the long-term, complex behavior of the seismic events. Considering the above-mentioned

filtering criteria, we kept in the statistics 4849 individual earthquakes for Romania, 66,948 for Japan and 22,848 for Southern-California.

The catalog we used for **Japan** is available at the JUNEK (Japan University Network Earthquake Catalog) web-page (*JUNEK web-page*). The database covers a time interval between 1985–1995. The values are given in the magnitude scale used by the JMA (Japan Meteorological Agency), called  $M_j$ . The conversion between  $M_j$  and  $M_w$  is given by the empirical formula (Utsu, 1982):

$$M_w = M_j - 0.171 . \quad (6)$$

The **Romanian** earthquake database, was granted by INFP (National Institute for Earth Physics). The magnitudes are given in the moment magnitude scale ( $M_w$ ). In order to ensure that the database is complete for events above the 2.5 magnitude, we used only the data between 2000 and 2018 (Moldovan et al., 2005).

The data for **Southern-California** was downloaded from the SCEDC (Southern California Earthquake Data Center) web-page (*SCEDC web-page*). We used the data between 1990 and 2019. This catalog uses the local magnitude ( $M_L$ ). Assuming earthquakes with magnitudes  $3 < M_L < 7$ , for Southern-California, the relation between  $M_L$  and  $M_o$  (Hanks and Kanamori, 1979; Thatcher and Hanks, 1973) suggests  $M_L = M_w$ , with a good approximation, since in the database there are only a few earthquakes with magnitude  $> 7$ , their effect on the statistics is therefore negligible.

In our data analyzing methodology the first step was to convert each and every magnitude value to  $M_w$ . Using now Eq. (2) with a constant multiplier factor (chosen as one) the corresponding total energy values were calculated. The investigated databases contained also the occurrence time moments for each earthquake, with a millisecond precision. These two properties (the total emitted energy and the occurrence time) were used to analyze different statistical properties.

#### 2.4. Results on the relevant statistics

Using the data presented in the previous section we have studied the magnitude distribution of earthquakes and the distribution of the recurrence times. Since we did not make any differentiation between fore-, after- and main shocks we did not investigate the rates of the aftershocks, and consecutively Omori's law. The results that are presented in the followings confirm again the validity of the known statistical laws. Moreover, the use of a consistent magnitude scale and the uniform filtering allowed us to uncover some useful universalities in the general statistics.

First, we constructed the mathematically well-defined probability density function (p.d.f.) for the dissipated energy distributions in all three tectonic re-

gions. The obtained results are summarized in Fig. 1. It can be clearly seen that the distributions belonging to different tectonic zones, collapse on a single master-curve, and can be well fitted by the Tsallis-Pareto (or Lomax II) p.d.f., with the following form:

$$\rho(E) = c \cdot \left(1 + \frac{E}{\lambda}\right)^{-1-b'}, \quad (7)$$

where  $b' = 0.6$ ,  $\lambda = 10^{3.45}$  (in energy dimensions) and  $c = 4.953 \times 10^{-4}$  (energy<sup>-1</sup> dimension) seem to be universal constants, independent of the investigated seismic region. The main motivation for the chosen fitting function instead of a simple power-law fit is its behavior in the small  $E$  limit. A simple power-law p.d.f cannot be normalized on the whole  $E > 0$  interval, it assumes a natural cutoff mechanism, and on a log-log scale it does not show the observed slope changes for small  $E$  values. The Tsallis-Pareto distribution is in the family of the q-exponential distributions (Tsallis, 2009), that are obtained from the maximization of the Tsallis entropy (Tsallis, 1988) under different constraints on the whole  $[0, \infty)$  interval. The Tsallis entropy generalizes the well-known Shannon entropy for processes where one cannot assume the extensivity of entropy. For multiplicative processes, where power-law distributions are dominant, the Tsallis-Pareto distribution usually offers a fair description of the observed statistics. Some examples are discussed in the review article of Biró and Nédá (2018).

The probability density function constructed for the used earthquake data, confirm on eight orders of energy magnitudes the validity of the Gutenberg-Richter law, and suggest an intriguing universality for the scaling exponent.

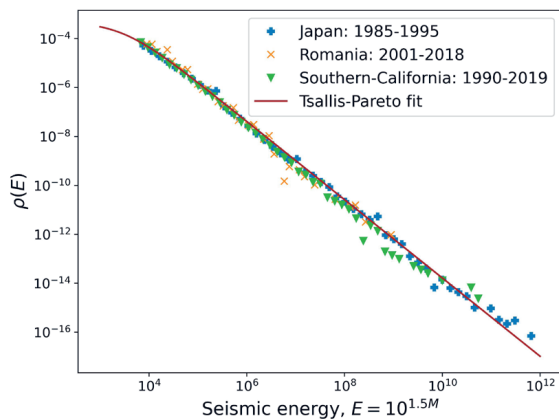


**Figure 1.** The probability density function for the seismic energy distributions for the studied tectonic zones on log-log scale. The clear scaling with exponent  $-1.6$ , on eight orders of magnitude proves the validity of the Gutenberg-Richter law and suggests the universality of the scaling exponent. Please note that according to Eq. (2) one needs a proportionality factor. In our case this was chosen as 1, fixing the unit for energy. In order to show the scaling, one does not need to specify the units used for energy.

For the recurrence time distribution, we aimed to find further universalities, allowing a connection between the statistics for large and small  $M_c$  thresholds. The motivation behind this is that due to the validity of the Gutenberg-Richter law there is a much worse statistics for the greater events, yet one is interested especially in the statistical aspects for such earthquakes. With this consideration we studied the recurrence time distribution, separately for the three tectonic regions, using several values for the threshold magnitudes. The Gamma distribution presented in Eq. (5), can be written for the  $t / \langle t \rangle$  rescaled time, where

$$\langle t \rangle = \frac{\alpha}{\beta} \quad (8)$$

is the average recurrence time. The p.d.f. for  $t / \langle t \rangle$  has in such case only one free parameter,  $\alpha$ :

$$\rho\left(\frac{t}{\langle t \rangle}\right) = \frac{\alpha^\alpha}{\Gamma(\alpha)} \left(\frac{t}{\langle t \rangle}\right)^{\alpha-1} e^{-\alpha\left(\frac{t}{\langle t \rangle}\right)}. \quad (9)$$

In the following we present on the same graphs the rescaled recurrence time distributions, obtained for different threshold magnitudes. Plots are on log-log scale and they are presented separately for each tectonic zone in part (Fig. 2). In these figures, the data points which belong to different threshold magnitudes are plotted with different colors and symbols. These, together with the parameter of the fitted Gamma distribution are specified in the legends of the figures. It is important to note that these distributions reflects also the Omori law (clustering phenomenon, after the great earthquakes) as a clearly distinguishable power-law trend in the  $t / \langle t \rangle \ll 1$  limit. One will immediately observe that for the fit with the Gamma function the  $\alpha$  parameter which characterizes the recurrence time distributions is always smaller than 1. This leads to an interesting, counter-intuitive conclusion for a given seismic zone. The probability of occurrence for an earthquake above a given magnitude in a fixed time interval (measured after the last such event) instead of increasing, will decrease in time (Corral, 2006).

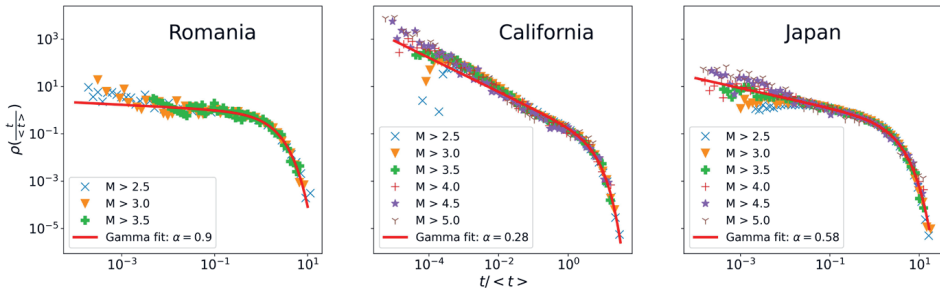


**Figure 2.** The recurrence time distributions (probability density functions) for the recurrence time rescaled with the mean. Different panels are for different seismologic regions as indicated on the graphs.

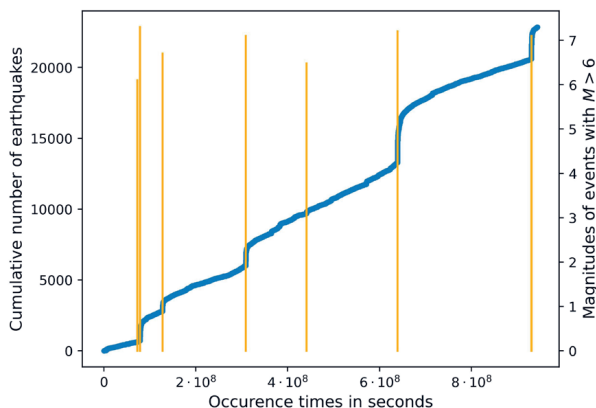


**Figure 3.** The cumulative number of earthquakes (dots) and the magnitudes of the events, for  $M_w > 6$  (vertical bars) as a function of their occurrence times (data for the Southern-California earthquake zone).

For  $\alpha = 1$  the Gamma distribution reduces to a simple exponential distribution, which indicates a Poisson process with no time-like correlations between the events. The difference relative to the  $\alpha = 1$  value characterizes the presence of correlations.

For illustrating more clearly the presence of the Omori law in our data, in Fig. 3 we present the cumulative number of earthquakes (blue dots) as a function of the occurrence time (the time elapsed since 1990/01/01 01:03:44.49 in seconds). On the same graph with the orange bars we present the magnitudes of earthquakes, selecting only those with  $M_w > 6$ . This graph is obtained for the Southern-California dataset. As one can clearly observe, after the large earthquakes there is an abrupt increase in the rate of the earthquake occurrences. This leads to the appearance of earthquake clusters, which are a manifestation of the Omori’s law.

### 3. Micro-scale quakes and their statistics

In the following the experimental study of micro-level “earthquakes” in metals are briefly presented and discussed. A more detailed discussion for the experiments can be found in the recent study of Ispánovity et al. (2022), uncovering also some similarities between earthquakes and dislocation motion induced avalanches in metals. We will use the same statistical analyses here as the one adopted for studying the earthquakes in the previous section.

In order to study the statistical properties of acoustic emission signals obtained during the deformation of metals one has to choose a suitable material and deformation mode for this task. The appropriate metal was selected based on its main deformation mechanism, which may also reflect on the strength of the acoustic activity. According to earlier investigations, fluctuations related to

sudden local strain bursts undergo a so-called wild-to-mild transition depending on the sample size (Weiss et al., 2015). Even single crystalline metals are characterized by a length-scale due to internal mechanisms such as interactions between dislocations and solute atoms (Weiss et al., 2021; Zhang et al., 2017), which act like motion barriers for dislocation movement, restricting the dissipated energy and number of produced acoustic signals. Specimens smaller than this scale exhibit scale-free fluctuations reminiscent to critical phenomena (wild regime), whereas in larger samples these fluctuations become weak/subcritical (mild regime). During the deformation of Faced-Centered Cubic (FCC) and Body-Centered Cubic (BCC) systems the avalanche numbers and sizes are highly temperature and sample size dependent (Alcala et al., 2020), which is mainly due to the strong influence of dislocation reactions and cross-slip phenomena on the dynamics. On the other hand, in pure Hexagonal Close Packed (HCP) single crystalline materials this length scale diverges, that is, large fluctuations are always observed, even for bulk samples. Therefore, Zn was chosen as a model material for studying micro-quakes.

### 3.1. Experimental details

A zinc single crystal (HCP structure) was obtained from Goodfellow Cambridge Ltd., with (10-11) surface normal direction. The compressions were carried out along the surface normal direction, meaning that the basal plane and the compression plane had an intersection angle of  $45^\circ$ , *i.e.* the single slip mechanism was favored during the experiments. The original crystal was embedded in polyacrylic resin (Dentacryl) and was cut into smaller samples using a diamond cutting disc. The samples were etched with  $\text{HNO}_3$  solution, before annealing. Heat treatment was carried out in a vacuum furnace for 6 hours on a temperature of  $150^\circ\text{C}$  and under a pressure of  $10^{-2}$  Pa. After the annealing, the samples were electropolished using electrolyte D2 from Struers, at a voltage of 12 V and maximum current of 1.5 A. Two samples of size  $6\text{ mm} \times 1.6\text{ mm} \times 1.6\text{ mm}$  and one of size  $8\text{ mm} \times 2.6\text{ mm} \times 2.6\text{ mm}$  were used for bulk compressions.

The micropillars were fabricated in a Quanta Fei 3D dual-beam scanning electron microscope (SEM) using the focused ion beam (FIB) technology. The fabrication was carried out using Ga ions by starting with a rough milling (30 kV, 10–15 nA) at low incidence angle ( $1^\circ$ – $2^\circ$ ) and ending with fine polishing (5 kV, 100 pA) at high angle of incidence ( $7^\circ$ – $8^\circ$ ). The side length of the prism shaped pillars having a square-shaped cross-section were  $8\ \mu\text{m}$ ,  $16\ \mu\text{m}$  and  $32\ \mu\text{m}$ , while the height was three times the side length. Figure 4 shows one of the compressed micropillars. In total, four  $8\ \mu\text{m}$ , three  $16\ \mu\text{m}$  and two  $32\ \mu\text{m}$  sized pillars were compressed, and statistical results are discussed for these.

In order to detect the micro-quakes during compression the phenomenon of acoustic emission was utilized. By definition, the phenomenon of acoustic emission is the generation of transient elastic waves during the irreversible struc-

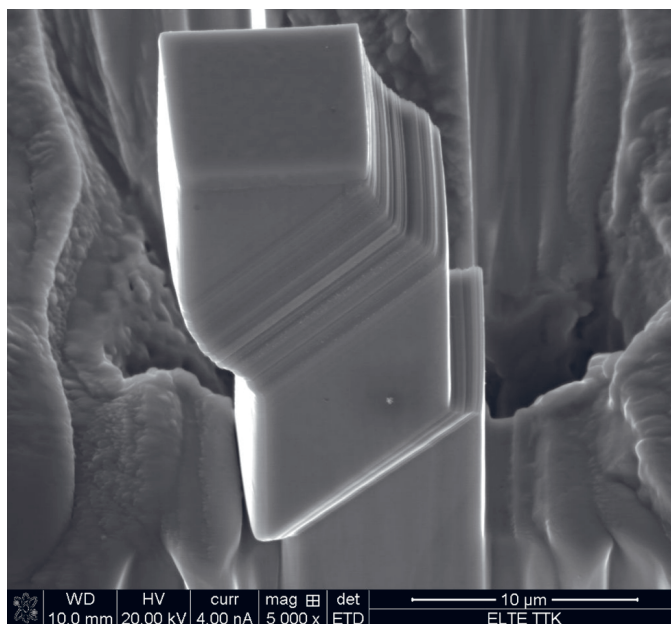


**Figure 4.** Secondary electron image of a compressed zinc micropillar with 8  $\mu\text{m}$  side length.

tural changes in materials. The component of the elastic waves which is perpendicular to the surface of the sample can be detected with piezoelectric transducers that are attached to the surface (or they are near the surface). In order to increase the efficiency of acoustic detection a layer of vacuum grease was applied between the sample and detector. The Acoustic Emission (AE) device consisted of a wide-band (100–1000 kHz) AE detector made by Physical Acoustic Corporation (PAC) W5a, a Vallen AEP5 40  $\text{dB}_{\text{AE}}$  pre-amplifier and the computer controlled Vallen AMSY-6 system, which was responsible for further amplification, continuous mode data-acquisition (at a rate of 2.5 MHz) and data processing. Acoustic Emission measurements were done simultaneously with the compression of samples. On Fig. 5a one can see the schematic drawing of a conventional stepper motor driven press for material testing procedures. This was used for the bulk samples. Since in this case the maximum stress applied to the system is in the range of hundreds of MPa, the exerted force on a millimeter sized area will be in the range of hundreds of N, corresponding to 10–100 kilogram-force. The AE detector would not withstand such a huge force, so instead of directly placing under the sample, it was positioned on the plunger as close as possible to the sample in order to avoid the dampening effect and the reflection generator nature of an interim medium. This type of compression can be considered a strain-controlled one, because one can assume that the elastic constant of the ram is infinitely high in comparison to that of the sample (the

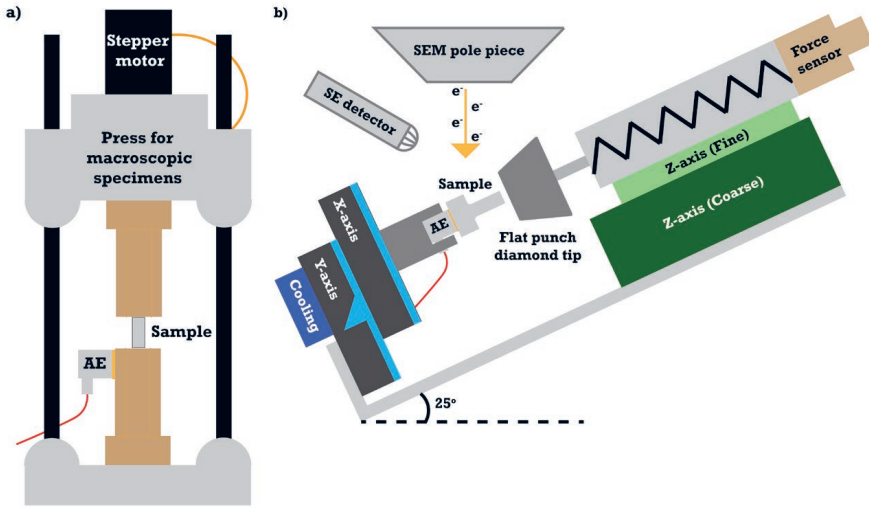


**Figure 5.** Schematic drawings of the *a)* stepper motor press and *b)* custom-made nano-indenter.

ram has a much larger tensile strength). The maximum *z*-axis resolution is approximately 10 nm.

For micropillars the experimental device allowed also in-situ SEM observation, and therefore the acoustic signals could be correlated with the observed slipping of the crystallographic planes (Máthis et al., 2021; Ispánovity et al., 2022). Figure 5b represents the schematic of the custom-made nano-indenter, which can be installed in the chamber of the SEM. This feature makes possible the observation and in-situ compression of micropillars. The “*x*-axis” and “*y*-axis” are positioning stages with precision of 0.5  $\mu\text{m}$ . The “*z*-axis (Coarse)” is a stepper

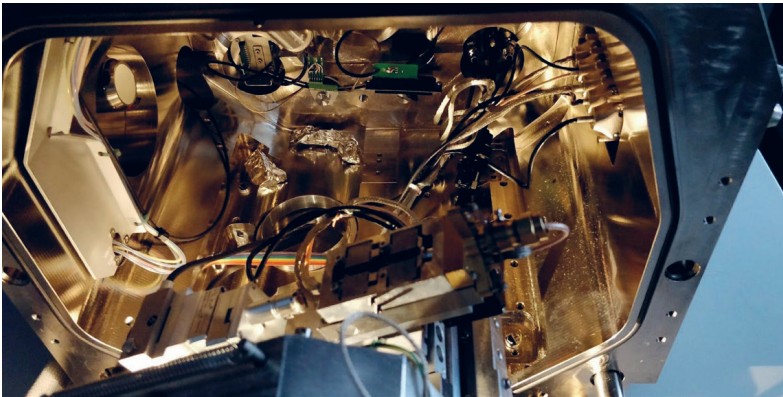


**Figure 6.** Photo of the custom made nano-indenter mounted on the stage of the SEM at open microscope chamber.

motor that allows the coarse positioning of the sample to the vicinity of the flat punch tip. On top of this, the “z-axis (Fine)” is a piezoelectric component, which upgrades the z-axis resolution to 1 nm. We have used this stage during the compression of the micropillars. A photo of the custom made nano-indenter mounted on the stage of the SEM at open microscope chamber is given in Fig. 6. Since the compressions were carried out with constant platen velocity, the system is again close to being strain-controlled (Ispánovity et al., 2022).

In Tab. 1 the used samples and corresponding deformation parameters are summarized.

*Table 1. The samples and compression rates used for the studies of avalanches induced by dislocation motion in metals.*

Sample	Dimensions	Strain rate (compression rate in mm/s)
Bulk Zn – nr. 1	8 mm × 2.6 mm × 2.6 mm	$6.25 \cdot 10^{-4}$ ( $5 \cdot 10^{-3}$ )
Bulk Zn – nr. 2	6 mm × 1.6 mm × 1.6 mm	$8.33 \cdot 10^{-4}$ ( $5 \cdot 10^{-3}$ )
Bulk Zn – nr. 3	6 mm × 1.6 mm × 1.6 mm	$3.33 \cdot 10^{-3}$ ( $2 \cdot 10^{-2}$ )
Micropillar Zn – nr. 1	8 μm × 8 μm × 24 μm	$8.33 \cdot 10^{-4}$ ( $2 \cdot 10^{-5}$ )
Micropillar Zn – nr. 2	16 μm × 16 μm × 48 μm	$4.12 \cdot 10^{-4}$ ( $2 \cdot 10^{-5}$ )
Micropillar Zn – nr. 3	32 μm × 32 μm × 96 μm	$2.08 \cdot 10^{-4}$ ( $2 \cdot 10^{-5}$ )

During data analysis, it was assumed that the energy  $E$  of acoustic signals are proportional to  $U^2$  where  $U$  is the electric potential difference, *i.e.* the amplitude of a single acoustic event produced in the piezoelectric acoustic sensor. Once the sensor produces an electric signal, it is pre-amplified and transmitted towards further amplification in order to allow a precise determination of the peak position and amplitude. The noise level of the measurement (*e.g.* the noise from the rotation of the stepper motor) is determined from preliminary measurements and a threshold value for peak identification is set appropriately. The exported data consists of peakwise data batches in the form of timeseries. From every batch the background threshold is set and the highest amplitude fluctuation is considered as the intensity of the signal. One could argue, that not only the highest fluctuation is responsible for the total dissipated energy. If ones take the squared valued signal, corresponding to dissipated energy timeseries and integrates, the area difference between the highest signal and the total data batch is insignificant. Nevertheless, before every batch of experiments the detectors are recalibrated with a pencil lead breaking test, which in ideal case produces a characteristic curve of the test (Sause, 2011; Yousefi, 2018). With this test, one can also check the reliability of the AE detectors, by comparing the results of several tests carried out successively.

During the compression of the bulk samples and micropillars the event rates change as a function of time during the compression. In Fig. 7 we show how the

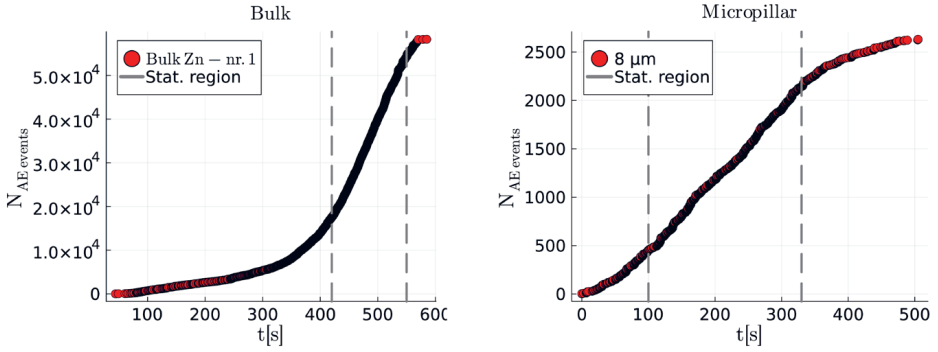


**Figure 7.** On the left side the cumulative number of AE events for Zn bulk compression as a function of time. The grey dashed lines mark the selected stationary region for analysis. On the right side the same graph for micropillar compression.

number of cumulative events depends on time for both bulk samples and micropillars. Several regions can be clearly distinguished as we indicate on the figure with dashed lines. In case of micropillars, the deformation is attributed purely to single slip on the basal plane, while for bulk crystals after a certain amount of time the single slip may dominate over other effects such as twinning. At the beginning, additional volume, surface and structure faults may dominate the dynamics, such as twinning or stacking fault. The statistics that will be presented and discussed in the following is based on the events detected in the region between the two dashed lines, where the rate of acoustic events is close to constant.

A common perception about acoustic emission phenomena detected in bulk samples is that the stress-time series and acoustic data do not exhibit any cor-

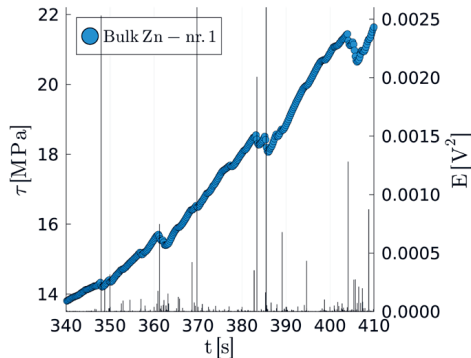


**Figure 8.** In case of single slip mechanism, even for bulk samples, there is a strong correlation between stress drops and acoustic events. Acoustic signals and their magnitude are presented with vertical bars.

relation in time. In other words, when an acoustic event occurs, the stress does not drop abruptly, but rather smoothly increases or fluctuates. In this case, since the crystal was intentionally oriented for single slip and forest dislocations are practically absent due to the HCP structure of Zn, strong correlations were detected in the stress-time series, even for bulk samples. This effect is illustrated in Fig. 8. Even more pronounced correlations are found for the compression of micropillars. Another common belief is that, although micropillars produce similar acoustic (microearthquake) statistics as earthquakes, due to the lack of spatial correlation these can be hardly compared to real earthquakes. Ispánovity et al. (2022) answered the question of spatial correlation via in-situ micropillar indentation and edge detection techniques.

### 3.1. Experimental results and relevant statistics

The experiments performed on bulk Zn samples proved nicely the validity of the Gutenberg-Richter law for the energy of the detected micro-quakes (Fig. 9). Using  $b' = 0.58$ ,  $\lambda = 5.4 \cdot 10^{-11} \text{ V}^2$  and  $c = 1.1 \cdot 10^8 \text{ V}^{-2}$  in Eq. (7) the observed data could be nicely fitted. We illustrate this fit by the dashed white line. The scaling with the exponent  $b' = 0.58$  is in good agreement with the scaling observed for earthquakes (Fig. 1), where we got the  $b' = 0.6$  exponent. For much smaller samples, *i.e.* using micro-pillars instead of the bulk samples it is possible also to study the size-effects. One would expect that for larger samples the statistics would be better and the power-law span a wider region. The very simple reason for this is that a controlled larger sample would allow larger slips. As it is shown in Fig. 9 (right-hand-side panel), the compression of micropillars with different sizes nicely confirm this prediction. It is interesting to note that the scaling exponent for the power-law tail remains invariant, with the same value as for bulk

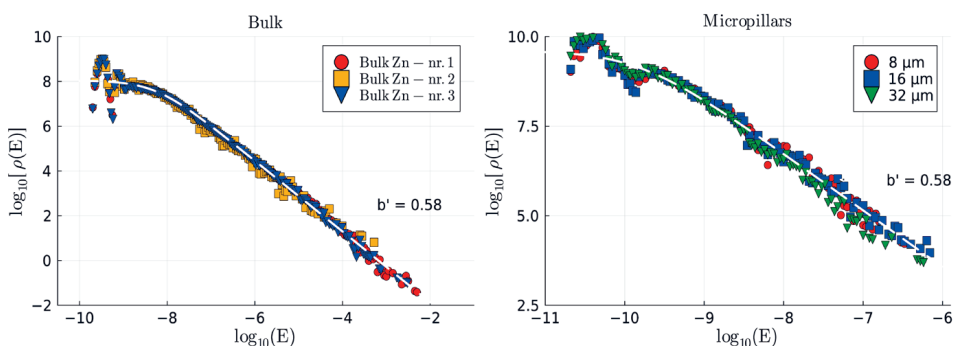


**Figure 9.** Probability density of acoustic event energies. On the left side the results obtained for bulk samples. The observed distribution is fitted with a Tsallis-Pareto type probability density function, with scaling exponent  $b' = 0.58$  (Eq. 9). On the right panel results for micropillars are shown. Compression of bigger pillars result in higher energy events, leading to longer power law tail.

samples. This is again a striking similarity with our finding for earthquakes in different seismologic regions.

We now turn our attention to the recurrence time statistics for the AE events. The same methodology that was applied for earthquakes is used. In Fig. 10 we plot the corresponding statistics for several AE energy threshold limits. Similarly to the statistics obtained for earthquakes, the distributions for different threshold values  $E$  collapse in the case of micropillars if we consider a rescaled recurrence time. Again, a clear power-law trend is present for low recurrence times which is related to the clustering effects in the system, expressed by the Omori-law. For this region in the case of bulk samples the governing exponent is  $p = 1.6$ – $1.8$ , slightly changing from experiment to experiment while for micropillars  $p = 1.2$ – $1.3$  is obtained. The large difference for the bulk from the  $p = 1$  value in the original Omori law confirms our previous assumptions that for the bulk sample although a single-slip dominated region was used in the statistics, other micromechanical effects (noise) may still be present in much stronger manner than in the case of micropillars. Another aspect worth of mentioning, is the fact that similarly to earthquakes  $\alpha < 1$  is consistently obtained for the Gamma distribution fits.

#### 4. Computational approach with the Burridge-Knopoff model

The Burridge-Knopoff spring-block model was introduced in the late 1960s by R. Burridge and L. Knopoff to model the phenomenon of earthquake production (Burridge and Knopoff, 1967). Our aim here is to reconsider the simple one-dimensional version of the model in view of the empirical results discussed

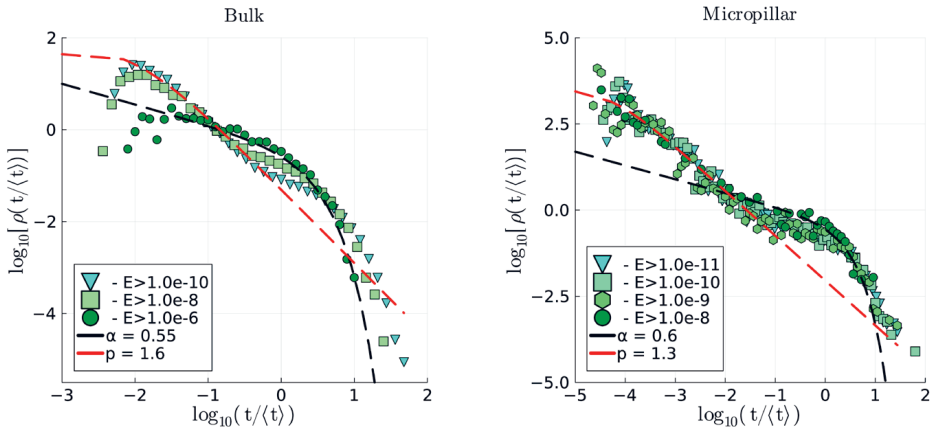


**Figure 10.** Recurrence time statistics for AE events for a given  $E$  threshold. The black dashed line indicates a fit with the Gamma distribution given in Eq. (11), and the red dashed line is a Tsallis-Pareto fit for the region where Omori's law is supposed to be valid. The  $p$  parameter is defined in Eq. (4). The left panel is for the bulk samples the right panel is for micropillars.

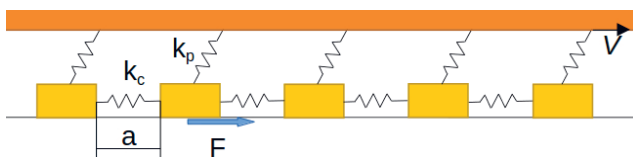


**Figure 11.** Schematic illustration of the main elements in a 1D Burridge-Knopoff model.

in the previous sections. The Burridge-Knopoff model uses a simple mechanical analogy to approach the dynamics of two interacting (slipping) “planes” and the phenomena of energy accumulation and release in such a process. The interaction between the planes and the accompanying plastic mechanical deformations are captured using an ensemble of blocks interconnected by springs as it is illustrated in Fig. 11. The motion of the blocks on the surface is friction-controlled, as it will be detailed in the followings. The model can be studied in the simple one-dimensional case or in the more realistic two-dimensional topology (Mori and Kawamura, 2008). We consider here a simple one-dimensional (1D) computational exercise. The reason for considering the 1D version of the model and not the 2D one is that for a proper statistics large systems and averages are needed. Our computational resources did not allow for running such ensembles in the more complex 2D topology.

#### 4.1. The 1D Burridge-Knopoff model

In the 1D topology a row of blocks with identical masses ( $m$ ) are placed on a plane. The blocks are attached to their neighbors by identical springs (having spring constant  $k_c$ ). There is a second plane above and every block is attached to this plane also by identical springs (with spring constant  $k_p$  in this case). The upper plane moves with velocity  $v$  and due to the interplay of the friction and elastic forces the blocks will have a complex stick-slip motion leading to avalanches of different sizes. Periods of potential energy accumulation (when the blocks are stationary on the bottom plane) and release (when some of the blocks slip to get in a more stable position) will continuously follow each other, leading to a typical SOC-like phenomenon.

The equation of motion of the  $j$ -th block is the following:

$$m\ddot{x}_j = k_c(x_{j-1} - 2x_j + x_{j+1}) - k_p x_j - F_f(v + \dot{x}_j) \quad (10)$$

where  $x_j$  denotes the position of the block  $j$  relative to its equilibrium position;  $F_f$  is the friction force (also called as the viscous term) which depends on the relative velocity of the planes  $v$ , and the velocity of block  $j$ .

From our viewpoint the relevant property of the system is its total potential energy. An analogy to an earthquake would be an avalanche-like decrease in the total potential energy, from a local maximum to the closest local minimum. It is

already known from the literature (Carlson and Langer, 1989) that this model leads to a Tsallis-Pareto-like energy distribution (which was obtained in the case of the real earthquakes as well). The main reason why we re-examine this model here is to learn whether it can also reproduce other relevant statistical features, like the seemingly general Gamma distribution for the recurrence times. Some properties of this 1D model have already been studied (see for example the work of Mori and Kawamura, 2006), therefore many of the results that we present are intended just for confirming earlier observations. In such cases we did however a more detailed mapping of the model's parameter space by attempting to get scaling exponents in agreement with the ones obtained for earthquakes and micro-quakes.

#### 4.2. Implementation

The Python programming language was used to numerically implement the previously described spring-block model. For solving the equations of motion, we used the well-known fourth-order Runge-Kutta method. The dimensionless form of Eq. (10) was used for the numerical implementation:

$$\ddot{U}_i = l^2(U_{i+1} + U_{i-1} - 2U_i) - U_i - \phi(2\zeta v + 2\zeta \dot{U}_i), \quad (11)$$

where  $U_i$  is the dimensionless displacement of the  $i$ -th block, relative to its equilibrium position,  $l = \sqrt{\frac{k_c}{k_p}}$  is the so-called stiffness parameter,  $v$  is the dimensionless relative velocity of the two planes. The parameter  $\zeta$  characterizes how the friction decreases with the increasing block velocity. According to the related scientific literature (Mori and Kawamura, 2006) we used the following velocity-weakening friction force:

$$\phi(z) = \begin{cases} f, & \text{if } f \leq 1 & z = 0 \\ 1, & \text{if } f > 1 & z = 0 \\ \frac{(1-\sigma)}{1+\frac{z}{1-\sigma}}, & & z > 0 \end{cases}, \quad (12)$$

where:  $z = 2\zeta v + 2\zeta(\dot{U}_i)$  and  $f = l^2(U_{i+1} + U_{i-1} - 2U_i) - U_i$ .

In the case of  $z = 0$ , if the resultant spring force has the same direction as velocity  $v$ , it will be completely compensated by the friction (this is applied in order to avoid the back-slip of the blocks). On the other hand, if  $z = 0$  and the direction of the resultant spring force is the opposite to  $v$  than it is compensated by the friction up to the value 1, and above the value 1, the friction has always unity value (this is basically due to the sticking part of the motion). Please note, that from here on all the used quantities and parameters are dimensionless and no units are therefore specified. Since we are interested only in scaling relations, such a numerical simplification is well-motivated and therefore acceptable.

There are two parameters that characterizes this velocity-weakening friction force: the  $\sigma$  which represents the drop in the friction force, when the respective block starts to slip (it was introduced by Carlson et al., 1991) and  $\zeta$  which characterizes how the friction decreases with the increasing block velocity. Totally, there are five parameters that can influence the behavior of the system:  $N$  (the number of block elements) and  $l, \zeta, \sigma, v$  which were previously mentioned.

As we already mentioned, we intend to follow the dynamics in the potential energy of the system, and to detect from here distinguishable avalanches that are associated with earthquakes. In Fig. 12 an example of a potential energy time series for the dynamics of the model is given. Generally, we observe that the energy drops from a local maximum to the closest local minimum, a process which is considered to be analogous to what happens both in earthquakes and dislocation motion. In order to clearly distinguish avalanches, we used the following restriction: when all of the blocks were stationary, the loading velocity ( $v$ ) was non-zero, and the elapsed simulation *time* (which is used as a variable to locate the occurrence times) passed uniformly (increased with a  $dt$  value in each and every numerical cycles). However, when one of the blocks started to slip, the value of  $v$  was set to 0, and also the elapsed simulation *time* was “frozen”. By this trick one could avoid that during an ongoing avalanche another one appears in a different part of the block chain. It allows also a clear time-like separation of different events. During such an avalanche the potential energy monotonically decreases.

Periodic boundary conditions were implemented and the first, unstable part of the time series was not considered in the statistics. During the simulations we recorded the variation of the total potential energy. The energy associated to

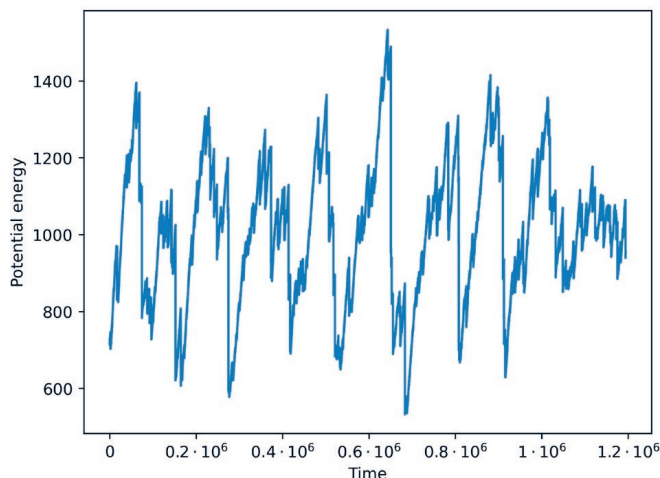


**Figure 12.** Example of the potential energy time series. The parameters in the simulation are:  $N = 6000$ ,  $l = 10$ ,  $v = 10^{-5}$ ,  $\zeta = 1$ ,  $\sigma = 0.01$ ,  $dt = 0.1$  (time step).

an avalanche was defined as the differences between the consecutive maxima and minima. We also recorded the occurrence times: the values of the previously described evolution *time*, at the starting points of the avalanches. Having in mind these we can conclude, that in Fig. 12 only the successive maxima and minima are in fact represented, since the intermediary steps are not important, and those were not even saved during the simulations.

### 4.3. Distribution of the dissipated energies

First, we wanted to assure that the size of the examined systems (the number of blocks,  $N$ ) are sufficiently large, to exclude finite size effects. We fixed:  $\nu=10^{-5}$ ,  $l=10$ ,  $\zeta=1$ ,  $\sigma=0.01$ ,  $dt=0.1$ , and studied the distribution of the energies in the avalanches for different system sizes between  $N=500$  and  $N=25000$ . The results presented in Fig. 13 suggest, that the obtained probability density functions for the energies of the detected avalanches do not differ substantially, therefore for  $N=6000$  the finite size effects can be already excluded. During our simulations we observed however, that the stiffness parameter,  $l$ , is the one that mostly influences the finite size effects. By increasing the value of  $l$ , the characteristic size of the avalanches increases, therefore larger systems are needed for eliminating finite size effects. Based on these observations we found that for  $l=10$ , one can use  $N=6000$  without being concerned for the finite size effects. In Fig. 13 one can observe the validity of the Guttenberg-Richer law on six orders of energy magnitudes. For the considered parameters the  $b' = 0.54$  scaling expo-

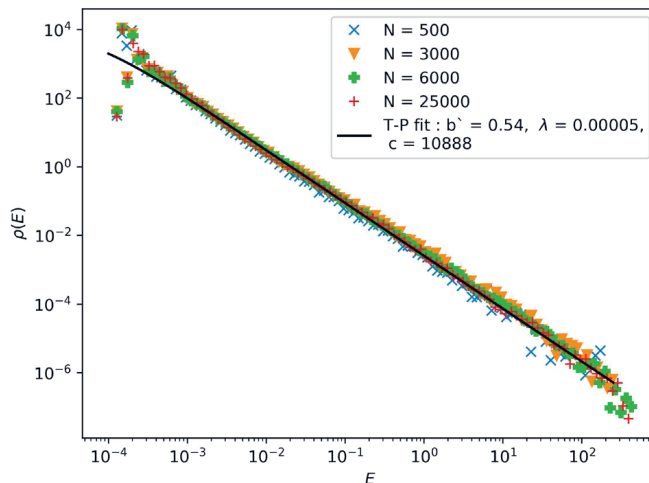


**Figure 13.** Probability density function for the energy distribution of the avalanches observed for the Burridge-Knopoff model. Simulation result for different system sizes,  $N$ , as shown in the legend. The solid line represents the Tsallis-Pareto fit with the parameters given in the legend. The other simulation parameters are:  $\nu=10^{-5}$ ,  $l=10$ ,  $\zeta=1$ ,  $\sigma=0.01$ ,  $dt=0.1$ .

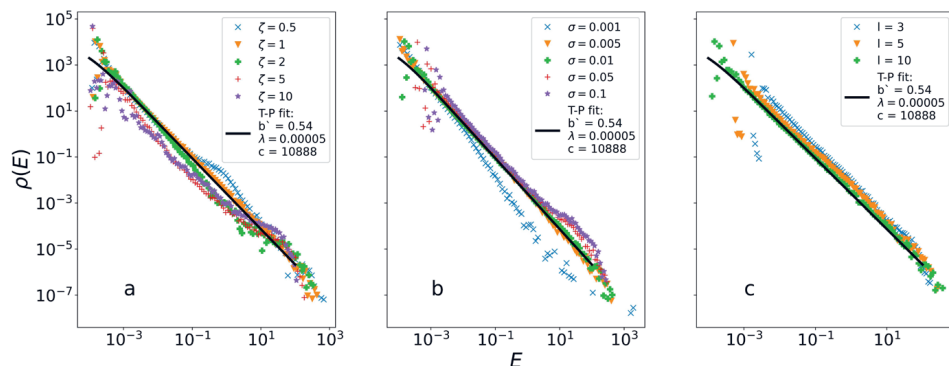


**Figure 14.** Probability density function for the energy distribution of the avalanches observed for the Burridge-Knopoff model. The influence of the  $\zeta$ ,  $\sigma$  and  $l$  parameters are shown on Figs. *a*, *b* and *c*, respectively. For Fig. *a* we have:  $l = 10$  and  $\sigma = 0.01$ , for Fig. *b*:  $l = 10$ ,  $\alpha = 1$ ,  $\zeta = 1$  and for Fig. *c*:  $\zeta = 1$  and  $\sigma = 0.01$ . The other parameters are fixed for:  $N = 6000$ ,  $\nu = 10^{-5}$  and  $dt = 0.1$ .

ment in a Tsallis-Pareto fit is very similar to the value  $\alpha = 0.6$  observed value for real earthquakes and  $b^* = 0.58$  observed for the micro-quakes.

Let us study now systematically the influence of the model parameters.

**a.** The  $\zeta$  parameter governs the friction force, and characterizes how the friction decreases with the increasing block velocity. By increasing the value of  $\zeta$  the friction decreases in a more accentuated manner with the velocity. The results obtained for different  $\zeta$  parameters (Fig. 14a) suggests that for  $\zeta = 1$  one can get similar distributions to the ones observed for earthquakes. For smaller or larger  $\zeta$  values, the energy distributions substantially differ from a Tsallis-Pareto distribution.

**b.** The  $\sigma$  parameter describes the drop in the friction force, which appears when a sticking block suddenly starts to slip. The results presented in Fig. 14b indicates that  $\sigma$  has also a major influence on the shape of the p.d.f.s for the energy distributions of the avalanches. The best scaling is for  $\sigma = 0.01$ . Interestingly, the influence of this parameter was not studied in the previous studies on the Burridge-Knopoff model.

**c.** The  $l$  parameter describes the stiffness of the spring-block chain. The results presented in Fig. 14c suggests that the characteristic exponents of the power law region for the p.d.f. are not influenced by the value of  $l$ . As it was already discussed, this parameter influences the cutoff in the scaling and consequently the finite-size effects.

#### 4.4. Recurrence time distribution

It is known from the early days of the Burridge-Knopoff model that it can reproduce successfully the Tsallis-Pareto-like p.d.f. for the dissipated energies.

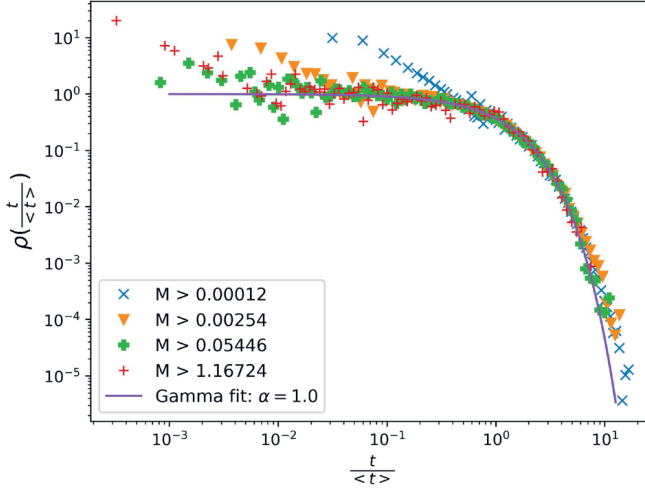


**Figure 15.** Recurrence time distributions in the simulated Burridge-Knopoff model. Results for different  $M$  thresholds. The other parameters of the simulations are:  $N=6000$ ,  $\nu=10^{-5}$ ,  $l=10$ ,  $\zeta=1$ ,  $\sigma=0.01$ ,  $dt=0.1$ .

Up to our knowledge, the recurrence time distributions were not studied within this model, so it is challenging to see whether the model is successful for reproducing also this stylized fact. We considered simulation for a broad range of model parameters, looking for reproducing the previously presented experimental results. Interestingly, we observed that for all the considered model parameters the results of the simulations were similar, leading to the recurrence time distribution presented in Fig. 15. Similarly, with the experimental results, different threshold magnitudes were implied, and the distributions for these were collapsed by renormalizing the time to the average value. The  $M$  threshold magnitudes were calculated as follows:  $M = \log_2(E)$ , similarly to real earthquakes ( $E$  represents the dissipated energy during the related event).

One will observe that the value of the fitting parameter for the Gamma-distributions is  $\alpha = \beta \approx 1$ , in all cases. In this limit the Gamma-distribution simplifies to the simple exponential distribution, which is specific to Poisson-like processes meaning lack of correlations between the large avalanches. It is also observable that similarly with the experimental data, in the limit of smaller recurrence times, our data does not follow the fitted Gamma-distribution, reaching higher probability density values and following a power-law trend. This indicates, that a clustering phenomenon is present at this scale, similarly with the Omori law observed for earthquakes and micro-quakes. Proceeding similarly with what has been done for earthquakes in Fig. 3, we can plot the cumulative number of events and their magnitudes as a function of the occurrence times to better visualize the clustering. This is done in Fig. 16. From this figure we ob-

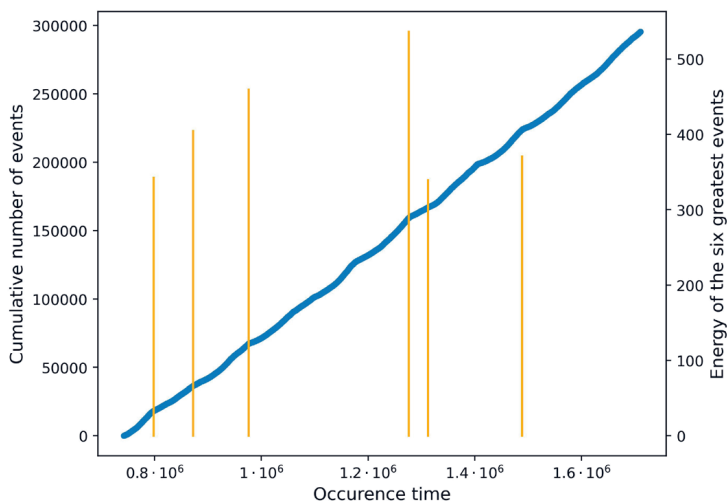


**Figure 16.** Cumulative number of events (dots) and the magnitudes of the six biggest simulated “earthquakes” (vertical bars) as a function of the occurrence time in the Burridge-Knopoff model. The model parameters are:  $N=6000$ ,  $\nu=10^{-5}$ ,  $l=10$ ,  $\zeta=1$ ,  $\sigma=0.01$ ,  $dt=0.1$ .

serve that there are no aftershock sequences, unlike for real earthquakes and micro-quakes in the deformation of metals. For earthquakes we observed that after a great earthquake, the rate of the detected earthquakes visibly increased, leading to the well-known Omori law. Instead of such an increase, here a decrease is observable right after the large avalanches. On the other hand, one can observe time periods with increased avalanche rates, but these are before the occurrence of the events with a large magnitude and not after them. This is a very different dynamical picture from the one offered in real earthquake dynamics, and suggests a critical self-organization before the occurrence of large block avalanches. This difference in the dynamical behavior is probably the result of the frozen simulation time, implied during an avalanche, necessary in order to clearly separate the events. We recall here, that in our computational model, several avalanches occurring at different places in the chain are taken together, as the simulation time is “frozen” until an avalanche stops. Seemingly this is the price one has to pay, for a simpler computational implementation of the Burridge-Knopoff model, without attempting a complicated de-clustering of the events. However, the critical self-organization observed before the occurrence of large avalanches, cannot be attributed to the chosen relaxation methodology.

## 5. Summary and conclusions

Three different, but seemingly strongly related physical phenomena leading to avalanche like processes were statistically analyzed: earthquakes in different seismotectonic areas, micro-quakes resulting from the slipping of crystallograph-

ic planes due to dislocation motion in metals and slipping of blocks in a stick-slip Burridge-Knopoff type model.

By using a proper energy scale for the energy dissipated in the avalanches we have shown the validity of the Guttenberg-Richter law on many orders of magnitude for the energy. The standardization of the magnitude scale allowed for collapsing the relevant probability density functions, and observing a universal scaling exponent for the power-law type tail. A Tsallis-Pareto type (Lomax II) probability density function with this universal exponent fitted excellently the data for earthquakes, micro-quakes and the stick-slip dynamics of the Burridge-Knopoff model. From the view of the energies dissipated in the avalanches these three phenomena are therefore analogous.

Evidences for the Omori law (aftershocks in form of avalanche clusters after a large event) were observed both for the studied earthquake databases and the acoustic recordings during the slipping dislocation planes. Although clustering of avalanches was observed in the dynamics of the Burridge-Knopoff model as well, these were shown to precede the large events, so they do not correspond to the conditions of the Omori's law.

The recurrence time of events above a given magnitude threshold was studied by following again the distribution for all three related phenomena. For earthquakes and micro-quakes, it was observed that for different magnitude thresholds their probability density function is well fitted with a non-trivial Gamma distribution. The distributions obtained for different magnitude thresholds collapse if we rescale the time with the average recurrence time. The 1D Burridge-Knopoff model shows similar statistics, although the fit parameters suggest here a trivial situation. One obtains an exponential distribution suggesting a total lack of correlations.

The statistical studies considered here lead to some clear overall conclusions. We proved that earthquakes and micro-quakes are clearly analogous phenomena, and the investigated statistics point not only to qualitative, but also to much deeper quantitative analogies. However, the 1D Burridge-Knopoff model which is extensively used for modeling earthquakes presents some deficiencies when one considers the time-like correlations between the events. The avalanche size statistics of this model reproduces elegantly the scaling in the Guttenberg-Richter law, but it fails to reproduce the Omori's law and the statistics observed in the recurrence times. This insufficiency is due to the lack of strong correlations in the system. Consequently, a step to be followed in modeling is to introduce some further elements in this simple model. Such endeavors were already explored, for example considering viscous coupling (Pelletier, 2000; Hainzl, 1999) is one successful route, where one can reproduce the Omori-law and certain important foreshock statistics as well.

*Acknowledgments* – The work of the team from the Babes-Bolyai University is supported by the UEFISCDI research grant: PN-III-P4-ID-PCE-2020-064. We thank dr. Mircea Radulian, the scientific director of the Național Institute for Earth Physics from Măgurele, Romania,

for providing the Romanian Earthquake dataset. The work of Attila Gergely is supported by the Collegium Talentum Programme of Hungary. Financial support from the National Research, Development and Innovation Fund of Hungary is also acknowledged (contract numbers NKFIH-K-119561 and NKFIH-FK-138975; S.L, D.U., P.D.I, and I.G.). Dávid Ugi was also supported by the ÚNKP-21-4 National Excellence Program of the Ministry for Innovation and Technology of Hungary. We acknowledge the helpful and relevant comments on behalf of the Editors.

## References

- Alcalá, J., Očenášek, J., Varillas, J., El-Awady, J. A., Wheeler, J. M. and Michler, J. (2020): Statistics of dislocation avalanches in FCC and BCC metals: Dislocation mechanisms and mean swept distances across microsample sizes and temperatures, *Sci. Rep.*, **10**(1), 1–14, <https://doi.org/10.1038/s41598-020-75934-5>.
- Bak, P., Tang, C. and Wiesenfeld, K. (1987): Self-organized criticality: An explanation of 1/f noise, *Phys. Rev. Lett.*, **59**(4), 381–384, <https://doi.org/10.1103/PhysRevLett.59.381>.
- Bak, P., Tang, C. and Wiesenfeld, K. (1988): Self-organized criticality, *Phys. Rev. A*, **38**(1), 364–374, <https://doi.org/10.1103/PhysRevLett.59.381>.
- Bak, P. and Chen, K. (1991): Self-organized criticality, *Sci. Am.*, **264**(1), 46–53.
- Biró, T. S. and Néda, Z. (2018): Unidirectional random growth with resetting, *Physica A*, **499**, 335–361, <https://doi.org/10.1016/j.physa.2018.02.078>.
- Bokelmann, G. and Rodler F.-E. (2014): Nature of the Vrancea seismic zone (Eastern Carpathians) – New constraints from dispersion of first-arriving P-waves, *Earth Planet. Sc. Lett.*, **390**, 59–68, <https://doi.org/10.1016/j.epsl.2013.12.034>.
- Bormann, P. and Saul J. (2009): Earthquake magnitude, in: *Encyclopedia of Complexity and Systems Science*, Vol. 3, edited by Meyers, A. Springer, New York, 2473–2496.
- Bormann, P. and Saul, J. (2011): *Earthquake magnitude. Extreme environmental events. Complexity in forecasting and early warning*. Springer, New York, 255–277.
- Bormann, P. (2011): Earthquake magnitude, in: *Encyclopedia of Solid Earth Geophysics*, edited by Gupta, H.K. Springer, Dordrecht, The Netherlands, 218–226.
- Bormann, P. and Dewey, J. W. (2014): The new IASPEI standards for determining magnitudes from digital data and their relation to classical magnitudes, in: *New Manual of Seismological Observatory Practice 2 (NMSOP-2)*, edited by Bormann, P. Potsdam, Deutsches GeoForschungsZentrum GFZ, 1–44.
- Burridge, R. and Knopoff, L. (1967): Model and theoretical seismicity, *Bull. Seismol. Soc. Am.*, **57**(3), 341–371, <https://doi.org/10.1785/BSSA0570030341>
- Britannica – Earthquake magnitude (2021): <https://www.britannica.com/science/earthquake-geology/Earthquake-magnitude>.
- Britannica – San Andrea fault (2021): <https://www.britannica.com/place/San-Andreas-Fault>.
- Britannica – Seismic wave (2022): <https://www.britannica.com/science/seismic-wave>.
- Carlson, J. M. and Langer, J. S. (1989): Properties of earthquakes generated by fault dynamics, *Phys. Rev. Lett.*, **62**(22), 2632–2635, <https://doi.org/10.1103/PhysRevLett.62.2632>.
- Carlson, J. M., Langer, J. S., Shaw, B. E. and Tang, C. (1991): Intrinsic properties of a Burridge-Knopoff model of an earthquake fault, *Phys. Rev. A*, **44**(2), 884–897, <https://doi.org/10.1103/PhysRevA.44.884>.
- Conti, L., Picozza, P. and Sotgiu, A. (2021): A critical review of ground based observations of earthquake precursors, in: *Geospace observation of natural hazards*, edited by Ouzounov, D., *Front. Earth. Sci., Sec. Geohazards and Georisks*, **9**, <https://doi.org/10.3389/feart.2021.676766>.
- Corral, Á. (2006): Statistical features of earthquake temporal occurrence, in: *Modelling critical and catastrophic phenomena in geoscience*, edited by: Bhattacharyya, P. and Chakrabarti B. K. Springer, Berlin, Heidelberg, 191–221.

- Dierke, H., Krawehl, F., Graff, S., Forest, S., Šachl, J. and Neuhäuser, H. (2007): Portevin–LeChatelier effect in Al–Mg alloys: Influence of obstacles—experiments and modelling, *Comp. Mater. Sci.*, **39**(1), 106–112, <https://doi.org/10.1016/j.commatsci.2006.03.019>.
- Dimiduk, D. M., Uchic, M. D. and Parthasarathy, T. A. (2005): Size-affected single-slip behavior of pure nickel microcrystals, *Acta Mater.*, **53**(15), 4065–4077, <https://doi.org/10.1016/j.actamat.2005.05.023>.
- Dimiduk, D. M., Woodward, C., LeSar, R. and Uchic, M. D. (2006): Scale-free intermittent flow in crystal plasticity, *Science*, **312**, 5777, 1188–1190, <https://doi.org/10.1126/science.1123889>.
- Earthquakes Booklet - How We Measure Them (2021): [http://earthquakes.bgs.ac.uk/education/eq\\_guide/eq\\_booklet\\_how\\_we\\_measure.htm](http://earthquakes.bgs.ac.uk/education/eq_guide/eq_booklet_how_we_measure.htm).
- El-Isa, Z. H. (2018): *Frequency-magnitude distribution of earthquakes*, in: *Earthquakes: Forecast, prognosis and earthquake resistant construction*, edited by Svalova, V. IntechOpen, London, p. 87–107.
- Groma, I. and Bakó, B. (2000): Dislocation patterning: From micro-to mesoscale description, *Phys. Rev. Lett.*, **84**(7), 1487, <https://doi.org/10.1103/PhysRevLett.84.1487>.
- Gutenberg, B. and Richter, C. F. (1944): Frequency of earthquakes in California, *Bull. Seismol. Soc. Am.*, **34**(4), 185–188, <https://doi.org/10.1785/BSSA0340040185>.
- Gutenberg, B. and Richter, C. F. (1956): Magnitude and energy of earthquakes, *Ann. Geophys.*, **9**(1), 1–15, <https://doi.org/10.4401/ag-5590>.
- Hainzl, S., Zöller, G. and Kurths, J. (1999): Similar power laws for foreshock and aftershock sequences in a spring-block model for earthquakes, *J. Geophys. Res.: Solid Earth*, **104**, B4, 7243–7253, <https://doi.org/10.1029/1998JB900122>.
- Hanks, T. C. and Kanamori, H. (1979): A moment magnitude scale, *J. Geophys. Res.: Solid Earth*, **84**, B5, 2348–2350, <https://doi.org/10.1029/JB084iB05p02348>.
- Hegyí, Á. I., Ispánovity, P. D., Knapék, M., Tüzes, D., Máthis, K., Chmelík, F., Dankházi, Z., Varga, G. and Groma, I. (2017): Micron-scale deformation: A coupled in situ study of strain bursts and acoustic emission, *Microsc. Microanal.*, **23**(6), 1076–1081, <https://doi.org/10.1017/S1431927617012594>.
- Hirsch, P. B. (1985): Dislocations in semiconductors, *Materials Science and Technology*, **1**(9), 666–677, <https://doi.org/10.1179/mst.1985.1.9.666>.
- Hutton, K., Woessner, J. and Hauksson, E. (2010): Earthquake monitoring in southern California for seventy-seven years (1932–2008), *Bull. Seismol. Soc. Am.*, **100**(2), 423–446, <https://doi.org/10.1785/0120090130>.
- Ispánovity, P. D., Ugi, D., Péterffy, G., Knapék, M., Kalácska, S., Tüzes, D., Dankházi, Z., Máthis, K., František Chmelík, F. and Groma, I. (2022): Dislocation avalanches are like earthquakes on the micron scale, *Nat. Commun.*, **13**, 1755, <https://doi.org/10.1038/s41467-022-29044-7>.
- JUNEC - Japan University Network Earthquake Catalog (2021): <http://wwwweic.eri.u-tokyo.ac.jp/CATALOG/junec/index.html>.
- Kalácska, S., Dankházi, Z., Zilahi, G., Maeder, X., Michler, J., Ispánovity, P. D. and Groma, I. (2020): Investigation of geometrically necessary dislocation structures in compressed Cu micropillars by 3-dimensional HR-EBSD, *Mater. Sci. Eng. A-Struct.*, **770**, 138499, <https://doi.org/10.1016/j.msea.2019.138499>.
- Lewis, J. (2005): Earthquake destruction: Corruption on the fault line, in: *Global Corruption Report*, edited by Transparency International. Pluto Press, London, pp. 23–30.
- Máthis, K., Knapék, M., Šiška, F., Harcuba, P., Ugi, D., Ispánovity, P. D., Groma, I. and Shin, K. S. (2021): On the dynamics of twinning in magnesium micropillars, *Materials & Design*, **203**, 109563, <https://doi.org/10.1016/j.matdes.2021.109563>.
- Matsu'ura, R. S. (2017): A short history of Japanese historical seismology: The past and the present, *Geosci. Lett.*, **4**(3), <https://doi.org/10.1186/s40562-017-0069-4>.
- Miguel, M., Vespignani, A., Zapperi, S., Weiss, J. and Grasso, J. R. (2001): Intermittent dislocation flow in viscoplastic deformation, *Nature*, **410**, 6829, 667–671, <https://doi.org/10.1038/35070524>.

- Moldovan, I. A., Popescu, E., Bazacliu, O., Enescu, B. D. and Radulian, M. (2006): Time, space and size distribution of earthquakes for Făgăraș seismogenic region (Romania), *Romanian J. Phys.*, **51**(3–4), 479–494.
- Mori, T. and Kawamura, H. (2006): Simulation study of the one-dimensional Burridge-Knopoff model of earthquakes, *J. Geophys. Res.: Solid Earth*, **111**, B7, <https://doi.org/10.1029/2005JB003942>.
- Mori, T. and Kawamura, H. (2008): Simulation study of the two-dimensional Burridge-Knopoff model of earthquakes, *J. Geophys. Res.: Solid Earth*, **113**, B6, <https://doi.org/10.1029/2007JB005219>.
- Ohnaka, M. (2013): *The physics of rock failure and earthquakes*, Cambridge University Press, p. 160–179, <https://doi.org/10.1017/CBO9781139342865>.
- Orowan, E. (1934): Zur Kristallplastizität. III, *Zeitschrift für Physik*, **89**(9), 634–659, <https://doi.org/10.1007/BF01341480>.
- Pelletier, J. D. (2000): Spring-block models of seismicity: Review and analysis of a structurally heterogeneous model coupled to a viscous asthenosphere, *Geophys. Monogr. – AGU*, **120**, 27–42, <https://doi.org/10.1029/GM120p0027>.
- Picozza, P. and Conti, L. (2021): Looking for earthquake precursors from space: A critical review, *Front. Earth Sci.*, **9**, 578, <https://doi.org/10.3389/feart.2021.676775>.
- Polanyi, M. (1934): Über eine Art Gitterstörung, die einen Kristall plastisch machen könnte, *Z. Phys.*, **89**(9), 660–664, <https://doi.org/10.1007/BF01341481>.
- Radulian, M. (2015): Mechanisms of earthquakes in Vrancea, in: *Encyclopedia of earthquake engineering*, edited by: Beer, M., Kougoumtzoglou, I. A., Patelli, E. and Au, S. K. Springer, Berlin, Heidelberg, [https://doi.org/10.1007/978-3-642-35344-4\\_302](https://doi.org/10.1007/978-3-642-35344-4_302).
- Richter, C. F. (1935): An instrumental earthquake magnitude scale, *Bull. Seismol. Soc. Am.*, **25**(1), 1–32.
- Sause, M. G. R. (2011): Investigation of pencil-lead breaks as acoustic emission sources, *J. Acoust. Emission*, **29**, 184–196.
- SCEDC – Southern California Earthquake Data Center (2021): [https://service.scedc.caltech.edu/ftp/catalogs/SCEC\\_DC/](https://service.scedc.caltech.edu/ftp/catalogs/SCEC_DC/).
- Taylor, G. I. (1934): The mechanism of plastic deformation of crystals. Part I.—Theoretical, *Proc. R. Soc. Lond. A*, **145**, 362–387, <https://doi.org/10.1098/rspa.1934.0106>.
- Thatcher, W. and Hanks, T. C. (1973): Source parameters of southern California earthquakes, *J. Geophys. Res.*, **78**(35), 8547–8576, <https://doi.org/10.1029/JB078i035p08547>.
- Topozada, T. and Branun, D. (2004): California earthquake history, *Ann. Geophys.*, **47**(2/3), 509–522, <https://doi.org/10.4401/ag-3317>.
- Tsallis, C. (1988): Possible generalization of Boltzmann-Gibbs statistics, *J. Stat. Phys.*, **52**(1–2), 479–487, <https://doi.org/10.1007/BF01016429>.
- Tsallis, C. (2009): Nonadditive entropy and nonextensive statistical mechanics – An overview after 20 years, *Braz. J. Phys.*, **39**, 337–356, <https://doi.org/10.1590/S0103-97332009000400002>.
- Tugui, A., Craiu, M., Rogozea, M., Popa, M. and Radulian, M. (2009): Seismotectonics of Vrancea (Romania) zone: The case of crustal seismicity in the foredeep area, *Romanian Rep. Phys.*, **61**(2), 325–334.
- Utsu, T. (1961): A statistical study on the occurrence of aftershocks, *Geophys. Mag.*, **30**, 521–605.
- Utsu, T. (1982): Relationships between earthquake magnitude scales, *Bull. Earthq. Res. Inst. Univ. Tokyo*, **57**, 465–497.
- Utsu, T. and Ogata, Y. (1995): The centenary of the Omori formula for a decay law of aftershock activity, *J. Phys. Earth*, **43**(1), 1–33, <https://doi.org/10.4294/jpe1952.43.1>.
- Weiss, J., Rhouma, W. B., Richeton, T., Dechanel, S., Louchet, F. and Truskinovsky, L. (2015): From mild to wild fluctuations in crystal plasticity, *Phys. Rev. Lett.*, **114**(10), 105504, <https://doi.org/10.1103/PhysRevLett.114.105504>.
- Weiss, J., Zhang, P., Salman, O. U., Liu, G. and Truskinovsky, L. (2021): Fluctuations in crystalline plasticity, *C. R. Phys.*, **22**(S3), 1–37, <https://doi.org/10.5802/crphys.51>.

- Wiemer, S. and Wyss, M. (2000): Minimum magnitude of completeness in earthquake catalogs: Examples from Alaska, the western United States, and Japan, *Bull. Seismol. Soc. Am.*, **90**(4), 859–869, <https://doi.org/10.1785/0119990114>.
- Yousefi, J., Mahdian, A., Karimi, Z. N., Heidary, H., Ahmadi, M. and Minak, G. (2018): Damage analysis for low velocity impacted composite laminates using acoustic emission technique, *FME Transactions*, **46**(2), 245–252, <https://doi.org/10.5937/fmet1802245Y>.
- Zhang, P., Salman, O. U., Zhang, J. Y., Liu, G., Weiss, J., Truskinovsky, L. and Sun, J. (2017): Taming intermittent plasticity at small scales, *Acta Mater.*, **128**, 351–364, <https://doi.org/10.1016/j.actamat.2017.02.039>.
- Zoller, K., Kalácska, S., Ispánovity, P. D. and Schulz, K. (2020): Microstructure evolution of compressed micropillars investigated by in situ HR-EBSD analysis and dislocation density simulations, *C. R. Phys.*, **22**(S3), 267–293, <https://doi.org/10.48550/arXiv.2011.08587>.
- Zöller, G., Hainzl, S., Kurths, J. and Zschau, J. (2002): A systematic test on precursory seismic quiescence in Armenia, *Nat. Hazards*, **26**(3), 245–263, <https://doi.org/10.1023/A:1015685006180>.

## SAŽETAK

## Statističke analogije između potresa, mikropotresa u metalima i lavina u 1D Burrridge-Knopoff modelu

*András Kuki, Sándor Lipcsei, István Gere, Ferenc Járαι-Szabó,  
Attila Gergely, Dávid Ugi, Péter Dusán Ispánovity, Zoltán Dankházi,  
István Groma i Zoltán Néda*

Univerzalnosti i intrigantne analogije u statistici lavina otkrivene su za tri fizička sustava definirana na uvelike različitim duljinama i energijskim skalama. Potresi uzrokovani dinamikom na tektonskoj skali, mikro-potresi koji nastaju na klizećim kristalografskim ravnina u metalima i jednodimenzionalni Burrridge-Knopoffov model opruga i blokova na skali sobe proučeni su sa sličnih statističkih stajališta. Valjanost Gutenberg-Richterove relacije za gustoću vjerojatnosti energija disipirane u lavinama dokazana je za sva tri sustava. Analizom podataka za tri različita seizmički aktivna područja i detekcijom akustičkih valova za različite uzorke Zn pod deformacijom, otkrivena je univerzalnost za uključeni eksponent skaliranja. S pravilnim izborom parametara 1D Burrridge-Knopoffov model može reproducirati isti zakon skaliranja. Vremena ponavljanja potresa i mikropotresa s magnitudama iznad zadanog praga opet predstavljaju slične distribucije i zapanjujuće kvantitativne sličnosti. Međutim, 1D Burrridge-Knopoffov model ne može objasniti korelacije opažene u takvim statistikama.

**Ključne riječi:** potresi, mikroplastičnost, lavine, univerzalnosti, skaliranje, korelacije, Burrridge-Knopoffov model

*Corresponding author's address:* Zoltán Néda, Physics Department, Babeş-Bolyai University, Cluj-Napoca, Romania; tel: +40 745 310 531; e-mail: zoltan.neda@ubbcluj.ro



This work is licensed under a Creative Commons Attribution-NonCommercial 4.0 International License.